

Supplementary Materials for

Birth of the East African Rift System: Nucleation of magmatism and strain in the Turkana Depression

Samuel C. Boone, Barry P. Kohn, Andrew J. W. Gleadow, Christopher K. Morley, Christian Seiler, and David A. Foster

This PDF includes:

Sample Collection and Methodology

Table DR1

Table DR2 and corresponding analytical protocols

Thermal History Modelling

Figures DR1 to DR9

References cited in Supplemental Material

SAMPLE COLLECTION AND METHODOLOGY

To constrain the low-temperature thermal history of the Lokichar Basin, Precambrian crystalline basement rock samples were collected from the western and eastern basin margins for apatite fission track (AFT) and (U-Th-Sm)/He (AHe) analyses. During field seasons in 2013 and 2015, ongoing tribal warfare in the region prevented the safe conduct of fieldwork in the Lokichar Basin western margin. Only in 2016, during a lull in local tensions, was limited access to the study area possible. Nevertheless, continued security issues significantly hindered field work south of 2° N 15', while sample collection to the north was limited by a scarcity of outcropping basement rock, largely obscured by Quaternary alluvium. Despite these impediments, eight samples were collected, including five samples from the Lokichar Fault footwall and three from the basin's flexural margin (Figs. 3 & DR6). Of the five footwall samples, three were collected in proximity (< 3 km) to the Lokichar Fault trace (11, 12 and 14). Two more (7 and 8) were sampled in the distal footwall, creating a pseudo-perpendicular transect to the Lokichar Fault trace that might elucidate any fault block tilting (Foster, 2018). A comprehensive review of the AFT and AHe methodologies and technical procedures used in this study can be found in Gleadow et al. (2015). A summary of the AFT and AHe analytical protocols are given in footnotes of Tables DR1 and DR2, respectively.

Data Reporting

AFT results and sample details, including rock types, coordinates and elevations, are listed in Table DR1. AHe data are presented in Table DR2. For simplicity, samples are referred to in the text and figures by the last digits of their sample code (i.e. 39 instead of TUB13-39) but are listed in full in the data tables. All ages are reported to one decimal place in the tables but rounded to whole numbers in the text, except for ages with 1σ errors <1 Ma. Dispersion in single grain AFT age populations are best explained by low precision of AFT age determinations for low uranium, and thus low fission track density grains (Figs. DR1 & DR2) (Vermeesch, 2018), and possibly the effects of REE substitutions on fission track annealing in Cl-poor grains (Figs. DR3 & DR4) (Barbarand et al., 2003). AFT ages are, thus, reported in the text as central ages. Samples 38 and 41 yielded insufficient apatite grains for He analysis. AHe ages for sample 8 (80 ± 5 to 161 ± 10 Ma) are significantly older than their corresponding AFT age (60 ± 3 Ma), despite having relatively low effective uranium (eU; $eU = U + 0.235 \cdot Th$) concentrations (4.3-7.7 ppm), suggesting that these ages may be erroneously old due to one of the many potential sources for dispersion (Wildman et al., 2016, Table 3). These are, therefore, omitted from interpretation and thermal history modelling. All remaining AHe ages exhibit no clear correlation to eU or grain size (Fig. DR5).

Table DR1. Lokichar Basin apatite fission track summary table

Sample No.	Rock Type	Longitude/Latitude	Elevation [m]	No. of grains	N_s	ρ_s [10^5 cm^{-2}]	^{238}U [ppm $\pm 1\sigma$]	Cl [wt%]	Dispersion [%]	$P(\chi^2)$	Pooled age [Ma $\pm 1\sigma$]	Central age [Ma $\pm 1\sigma$]	N_{length}	Mean track length [$\mu\text{m} \pm \text{se}$]	St.Dev. [μm]
Lokichar Basin Footwall															
Distal Lokichar Fault Footwall															
TUB16-7	Biotite-Granulite	35.59524/2.32415	846	30	3492	7.3648	28.8 ± 10.32	0.28	11	0.00	53.9 ± 1.8	54.4 ± 1.6	100	13.3 ± 0.2	1.56
TUB16-8	Biotite-Granulite	35.57142/2.28210	837	30	760	2.0687	7.16 ± 3.02	0.03	18	0.01	58.4 ± 3.8	60.4 ± 3.2	100	12.4 ± 0.2	1.82
Proximal Lokichar Fault Footwall															
TUB16-11	Granulitic gneiss	35.72054/2.17156	907	28	645	1.5397	8.52 ± 4.46	0.11	21	0.00	38.1 ± 2.9	40.6 ± 2.4	100	13.0 ± 0.2	2.10
TUB16-12	Granulitic gneiss	35.72213/2.17118	837	25	987	2.2584	16.32 ± 13.87	0.08	20	0.00	34.5 ± 2.3	35.8 ± 2.0	100	13.6 ± 0.2	1.75
TUB16-14	Granulitic gneiss	35.65581/2.44495	770	27	316	1.3894	10.89 ± 5.99	0.04	22	0.04	28.6 ± 2.2	29.3 ± 2.2	100	13.5 ± 0.2	1.93
Lokichar Basin Flexural Margin (Lokone Horst)															
TUB13-38	Jarner Granulitic Gneiss	35.973534/2.412424	621	12	47	0.6504	2.37 ± 1.37	0.01	0	0.96	60.0 ± 7.1	62.7 ± 10.0	-	- \pm -	-
TUB13-39	Biotite Gneiss	35.984500/2.519400	632	23	1621	7.8726	33.4 ± 22.11	0.06	36	0.00	53.6 ± 6.2	56.2 ± 4.9	176	11.9 ± 0.2	2.01
TUB13-41	Biotite Gneiss	35.958500/2.516400	645	7	59	2.8997	17.5 ± 24.90	0.14	62	0.00	46.1 ± 18.1	60.1 ± 17.8	-	- \pm -	-

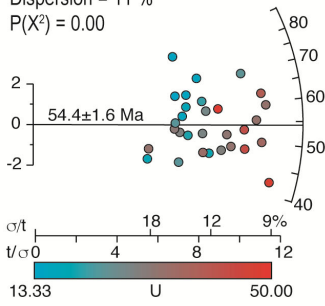
Notes: Apatite grains were mounted and polished, and fission tracks analysed using the LA-ICP-MS technique following procedures described in *Gleadow et al.* [2015]. Analyses were performed by SCB on image sets captured by TrackWorks using a 3.2MP AVT Oscar F-320C camera mounted on a Zeiss AxioImager microscope with a 1000x total magnification and a 100x dry objective (calibration = 0.07 μm by 0.07 μm per pixel). Spontaneous track densities were measured on prismatic internal apatite surfaces after etching with 5M HNO_3 for 20sec at 20°C. Track counts were obtained by automated counting in FastTracks using the 'coincidence mapping' technique of *Gleadow et al.* [2009] followed by manual inspection. Uranium concentrations of each grain were determined by LA-ICP-MS single spot analysis using a New Wave Nd:YAG Laser ($\lambda=213\text{nm}$ with 5Hz @ 45% power, spot size=30 μm) connected to an Agilent 7700 mass spectrometer. NIST612 was used as the primary reference material and a sintered Mud Tank Carbonatite apatite as an in-house secondary reference material during LA-ICP-MS analyses, following the protocol of *Boone et al.* [2016]. Data reduction of LA-ICP-MS results were performed using the TraceElementst_IS data reduction scheme in software package lolite [*Paton et al.*, 2011]. Single grain and pooled ages were calculated according to *Hasebe et al.* [2004]. Central ages were estimated from single grain ages and errors according to the formulas given by *Galbraith* [2005, p.100] using the Newton-Raphson method. All ages are "model" ages obtained using a range factor (R_s) of 7.17 μm and are directly comparable to conventional External Detector Method ages [*Seiler et al.*, 2014]. Confined track lengths (TINTs) were measured as true 3D lengths using *FastTracks* after irradiation by ^{252}Cf and are corrected for a refractive index of 1.634 for apatite. Chlorine concentrations of individual apatite grains were measured using a Cameca SX50 electron microprobe.

N_s = number of spontaneous tracks counted; ρ_s = spontaneous track density; $P(\chi^2)$ = Chi-square probability; N_{length} = number of lengths measured; se = standard error

Distal Footwall Samples

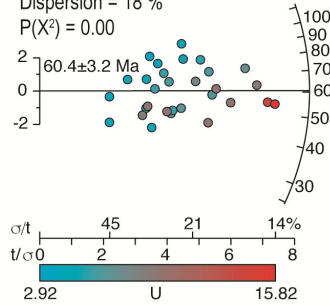
TUB16-07 (n = 30)

Dispersion = 11 %
 $P(X^2) = 0.00$



TUB16-08 (n = 30)

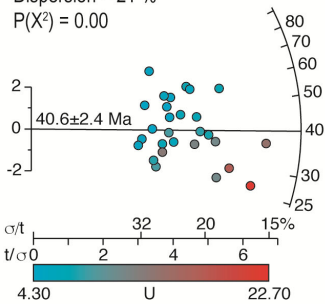
Dispersion = 18 %
 $P(X^2) = 0.00$



Proximal Footwall Samples

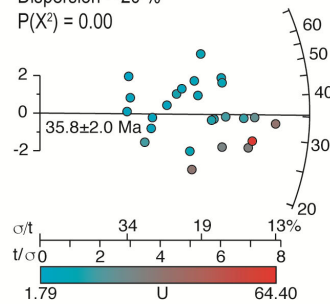
TUB16-11 (n = 28)

Dispersion = 21 %
 $P(X^2) = 0.00$



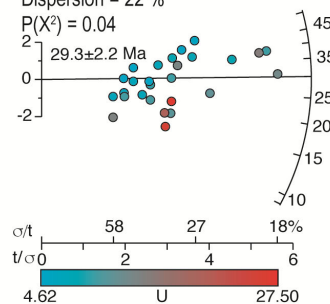
TUB16-12 (n = 25)

Dispersion = 20 %
 $P(X^2) = 0.00$



TUB16-14 (n = 27)

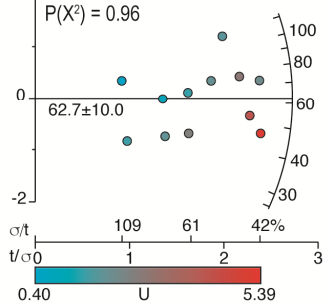
Dispersion = 22 %
 $P(X^2) = 0.04$



Hanging Wall Samples

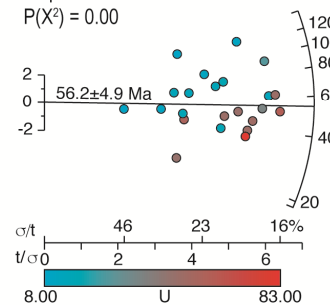
TUB13-38 (n = 12)

Dispersion = 0 %
 $P(X^2) = 0.96$



TUB13-39 (n = 23)

Dispersion = 36 %
 $P(X^2) = 0.00$



TUB13-41 (n = 7)

Dispersion = 62 %
 $P(X^2) = 0.00$

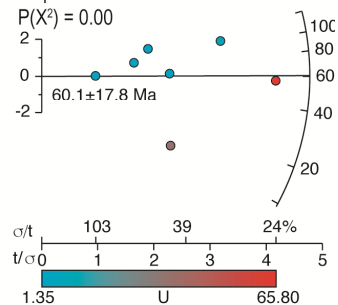


Figure DR1. Single grain AFT age distributions and uranium content. Radial plots were constructed using *Radial Plotter* (Vermeesch, 2009). The age for each point on a radial plot is obtained by projecting a line from the origin through the single grain age (circles) to the radial age axis. All points have the same error bar indicated by the axis about the origin on the left ($\pm\sigma$). The further a point plots to the right, the more precise the single grain age, as seen by the horizontal precision axis directly below the plot. The color assigned to each age shifts from blue to red with increasing U content (ppm).

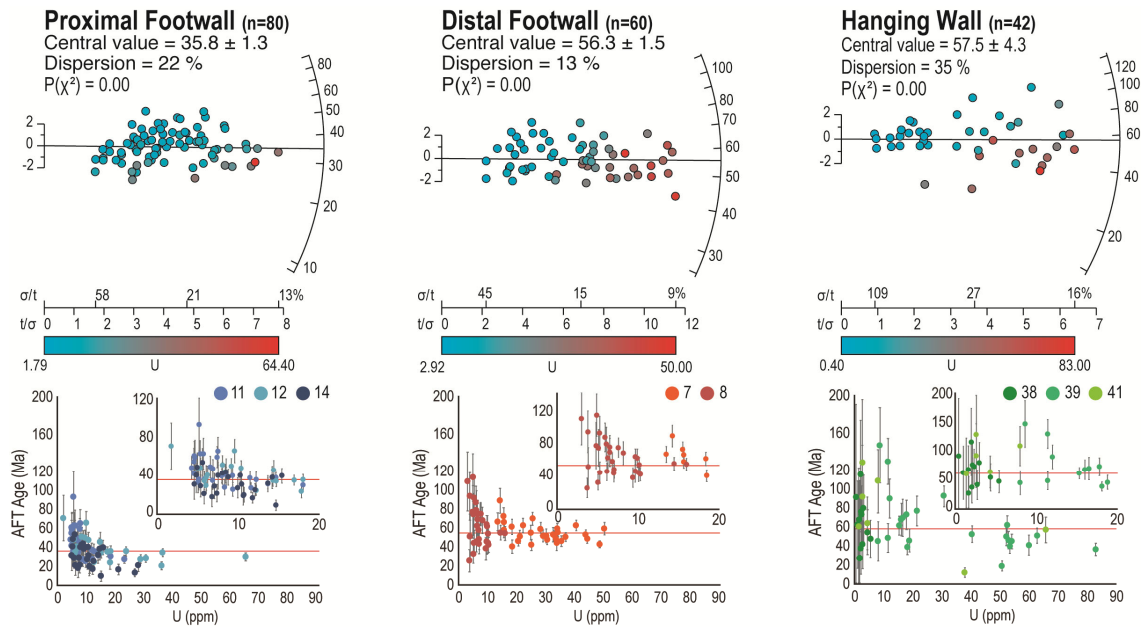
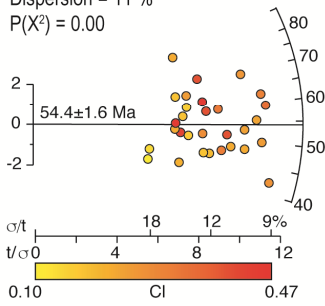


Figure DR2. Radial (upper row) and scatter plots (lower row) of single grain AFT ages [Ma] with respect to U content [ppm] for proximal footwall (11, 12 and 14), distal footwall (7 and 8), and hanging wall samples (38, 39 and 41). See caption of Fig. DR1 for description of radial plots, constructed using *Radial Plotter* (Vermeesch, 2009). Low uranium, and hence low fission track density, single grain AFT ages may exhibit a marked increase in dispersion. Nevertheless, many of the dispersed grains are still within 1σ (error bars) of the central AFT age (red line) of their respective sample group (proximal footwall, distal footwall and hanging wall).

Distal Footwall Samples

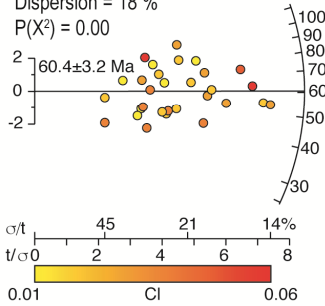
TUB16-07 (n = 30)

Dispersion = 11 %
 $P(X^2) = 0.00$



TUB16-08 (n = 30)

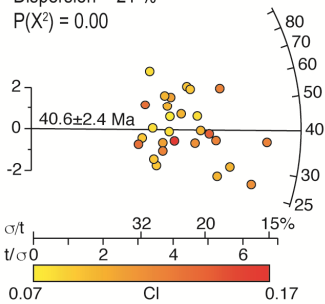
Dispersion = 18 %
 $P(X^2) = 0.00$



Proximal Footwall Samples

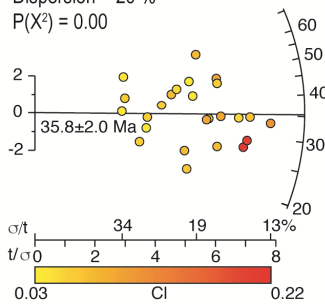
TUB16-11 (n = 28)

Dispersion = 21 %
 $P(X^2) = 0.00$



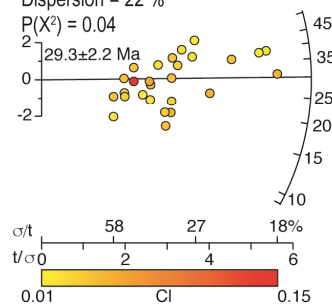
TUB16-12 (n = 25)

Dispersion = 20 %
 $P(X^2) = 0.00$



TUB16-14 (n = 27)

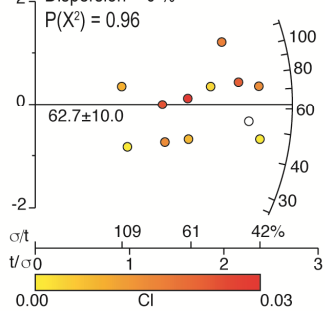
Dispersion = 22 %
 $P(X^2) = 0.04$



Hanging Wall Samples

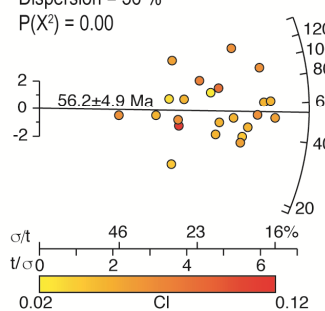
TUB13-38 (n = 12)

Dispersion = 0 %
 $P(X^2) = 0.96$



TUB13-39 (n = 23)

Dispersion = 36 %
 $P(X^2) = 0.00$



TUB13-41 (n = 7)

Dispersion = 62 %
 $P(X^2) = 0.00$

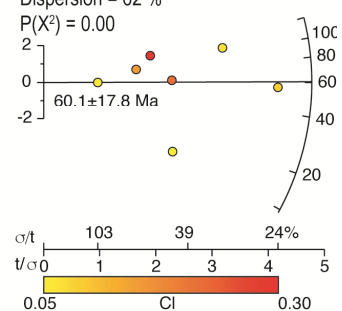


Figure DR3. Single grain AFT age distributions and chlorine content. See caption of Fig. DR1 for description of radial plots generated using *Radial Plotter* (Vermeesch, 2009). The color assigned to each age shifts from yellow to red with increasing Cl content (wt%).

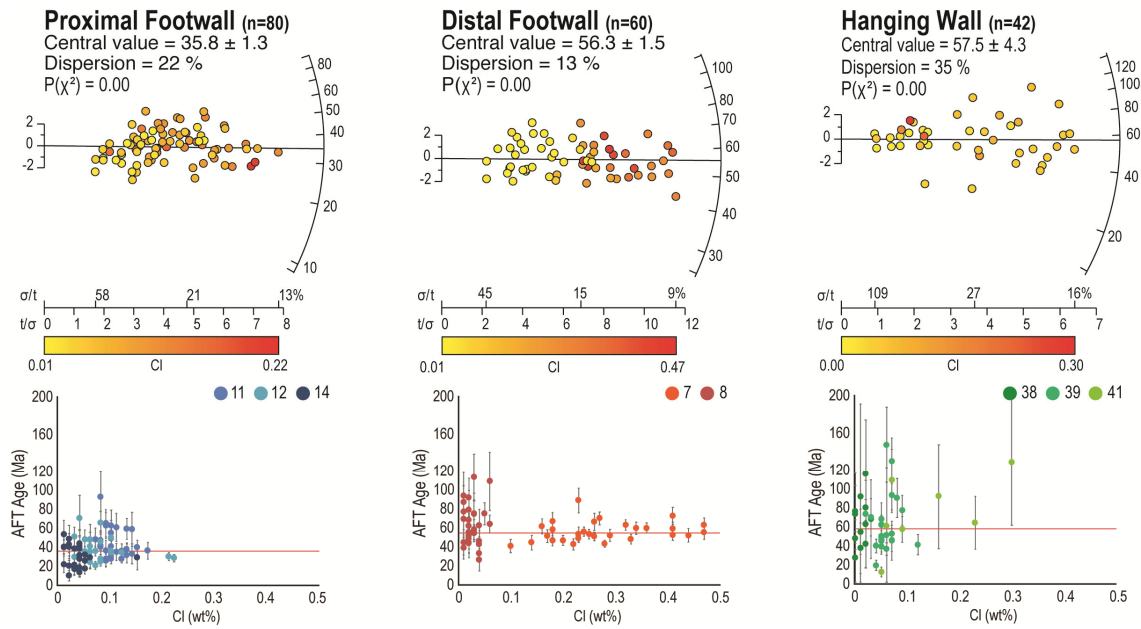


Figure DR4. Radial (upper row) and scatter plots (lower row) of single grain AFT ages [Ma $\pm 1\sigma$] with respect to Cl content [wt%] for proximal footwall (11, 12 and 14), distal footwall (7 and 8), and hanging wall samples (38, 39 and 41). See caption of Fig. DR1 for description of radial plots, constructed using *Radial Plotter* (Vermeesch, 2009). Lower Cl grains, particularly in distal footwall and hanging wall sample, may exhibit a marked increase in AFT age dispersion, perhaps reflecting the significance influence that elemental substitutions in apatite crystal, namely LREE, can have on fission track annealing in Cl-poor apatites (Barbarand et al., 2003). Red lines represent central AFT ages of proximal footwall, distal footwall and hanging wall sample groups.

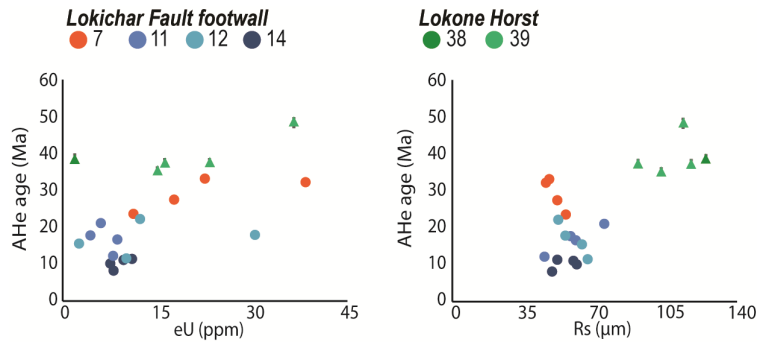


Figure DR5. Single grain AHe ages versus effective uranium ($eU = U + 0.235 \cdot Th$; left plot) and Equivalent Spherical Radius ($R_s = [3 \cdot R \cdot L] / 2 \cdot [R + L]$, where R is grain radius and L is grain length; right plot).

THERMAL HISTORY MODELLING

In order to quantify thermal histories for basement samples from the footwall of the Lokichar Fault, AFT and AHe data were jointly inverse (Figs. DR6 & 7) and forward modelled (Figs. DR8 & 9) using the software *QTQt* (Gallagher, 2012), with the multi-compositional fission track annealing model of Ketcham et al. (2007a). *QTQt* employs a Bayesian transdimensional Markov chain Monte Carlo (MCMC) sampling method to generate a range of acceptable thermal histories, quantified in terms of a posterior probability distribution (Gallagher et al., 2009; Gallagher 2012). Confined fission track lengths were normalised for annealing and etching anisotropy using the c-axis projection method (Ketcham et al., 2007b). Large analytical uncertainties for low-U, low fission track density grains and the effects of apatite composition on fission track annealing (Barbarand et al., 2003) are accounted for during thermal history modelling, as single grain AFT data are modelled together with their corresponding U and Cl concentrations. Samples that did not yield confined fission track measurements (38 and 39) were omitted during thermal history modelling. A radiation damage accumulation and annealing model was employed for modelling of AHe data (Gautheron et al., 2009) to account for differences in radiation-modified diffusion kinetics. For samples with fragmented AHe grains, only 1- and 2-termination grains were modelled in *QTQt* due to the current implementation of the Brown et al. (2013) fragmentation model being unable to model 0T grains.

Inverse Thermal History Modelling

A temperature range of 0-140 °C and a time range of 0 Ma to twice the value of the oldest thermochronometer age were used for the time-temperature prior range. During thermal history modelling of individual samples, 150,000 iterations were run, with the first 50,000 discarded as burn-in (Gallagher et al., 2009). To ensure satisfactory sampling, the acceptance rates of the proposed model parameters and the posterior sampling chain were checked after each modelling run (Gallagher, 2012). A time-temperature constraint was also applied to all models, requiring samples to be at a present-day surface temperature of 20 ± 10 °C. In all cases, inverse thermal history modelling was able to reproduce observed AFT data. Where inverse models were unable to also reproduce AHe data (samples 7 and 39), inverse modelling then performed using AFT data alone for comparison.

Forward Thermal History Modelling

Forward thermal history modelling was performed with *QTQt* to calculate AFT and AHe data based on a series of geologically plausible, prescribed thermal histories. These included monotonic and 2-stage Late Cretaceous-Recent cooling (orange and red t-T paths in Fig. DR4), simulating pervasive Late Cretaceous-Paleogene cooling recorded regionally (see text) and consistent with the inverse thermal history models of samples 7, 8 and 39 (AFT data alone). In addition, Lokichar Basin formation-related thermal history scenarios were modelled, involving either a late Paleogene transition to relatively rapid cooling associated with Lokichar Fault footwall uplift and denudation (samples 7, 8, 11, 12 and 14), or, for sample 39, a period of late Tertiary reheating in response to burial of the Lokichar flexural margin beneath syn-rift strata and/or a period of middle Miocene volcanism restricted to the basin's eastern margin (Morley et al., 1999). To further constrain the timing of any rift-related thermal event recorded along the Lokichar Basin margins, the onset of late Paleogene-Miocene cooling was also varied between models by increments of 5 Ma, from 30 Ma (age of oldest, exposed syn-rift Lokichar strata; Morley et al., 1999) to 55 Ma (Fig. DR4). For samples 7 and 8, whose older AFT ages and more moderate MTL record more prolonged residence in the AFT partial annealing zone (~60-120 °C; e.g. Wagner and van den Haute,

1992), the maximum paleotemperatures prior to the onset of cooling related to Lokichar Basin formation were reduced, preceded by more gradual Late Cretaceous-Paleogene cooling. In other words, we tested whether the thermochronology data of samples 7 and 8 are consistent with a late Paleogene transition to more rapid cooling in response to Lokichar Basin formation, albeit of lower amplitude than that experienced by their proximal footwall counterparts. In all cases, prescribed cooling histories began at 120 °C, the approximate bottom of the AFT partial annealing zone (e.g. Gleadow and Duddy, 1981).

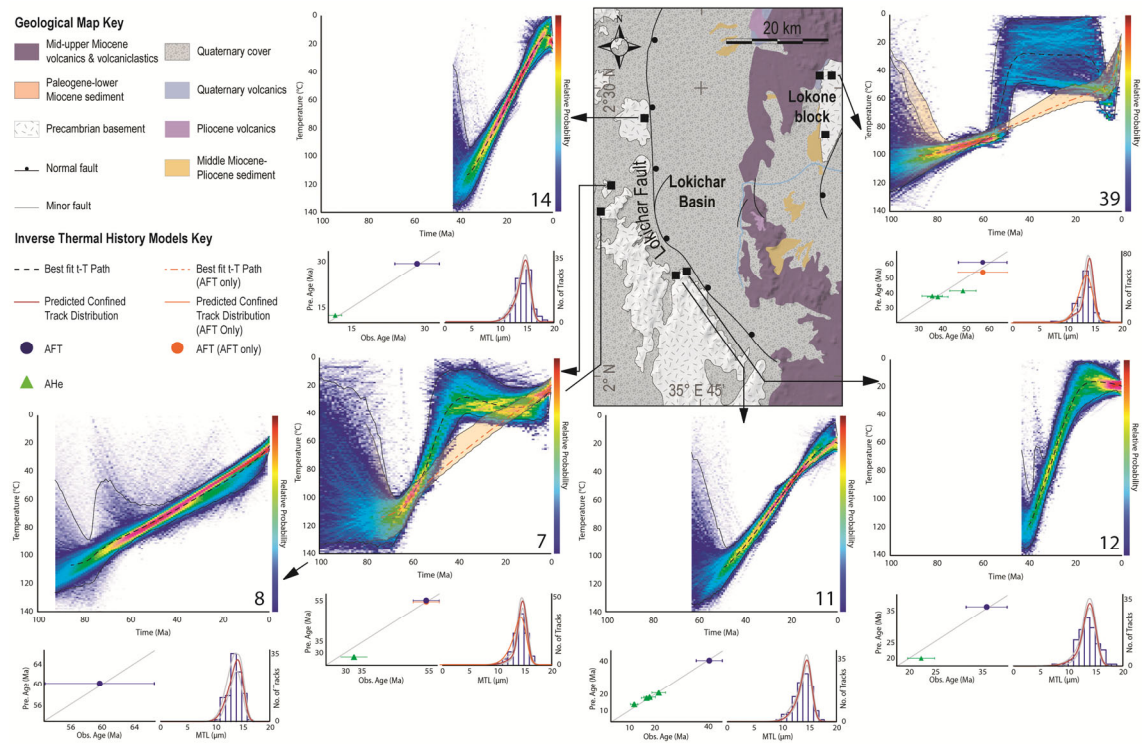


Figure DR6. Inverse time-temperature histories of basement samples from the Lokichar Basin margins, determined using *QTQt* (Gallagher, 2012). See Thermal History Modelling for detailed modelling procedure. The color map represents the posterior-probability distribution of accepted time-temperature paths, with warmer colours indicating higher probabilities. The best-fit time-temperature paths (weighted mean of the posterior distribution; see Gallagher, 2012 for discussion) are represented by black dashed lines. Black solid lines represent the 95% confidence interval limits. The data fit for each thermal history model is illustrated by panel inserts showing observed versus predicted thermochronology ages (note that He ages are displayed with resampling errors) and observed confined track distributions overlain by the predicted distributions (red curve) and the 95% confidence interval (grey curves) of the predicted distributions. Where inverse models were unable to reproduce AHe ages (samples 7 and 39), the results of inverse thermal history modelling of AFT data alone are also shown in orange (orange envelope represents the 95% confidence interval). Models for distal footwall samples 7 (only AFT) and 8 record monotonic Late Cretaceous-Recent cooling. By contrast, models for proximal Lokichar Fault footwall samples (11, 12 and 14), record pronounced Eocene to Miocene cooling. The model of sample 39 (only AFT) exhibits gradual Late Cretaceous-Miocene cooling, similar to the models of samples 7 and 8, followed by late Miocene-Recent rapid cooling. Geological map, after BEICIP (1987), showing sample localities and underlain by a digital elevation model (NASA, 2000).

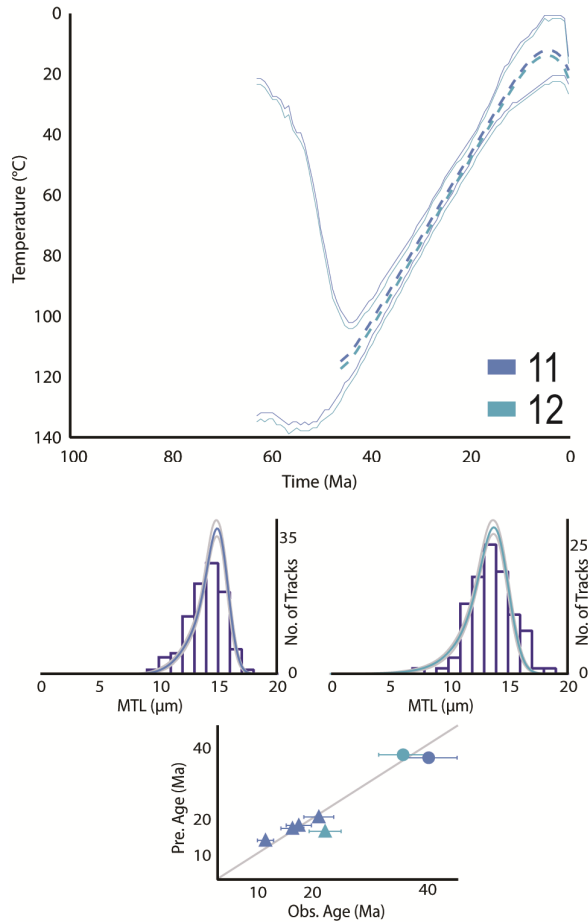
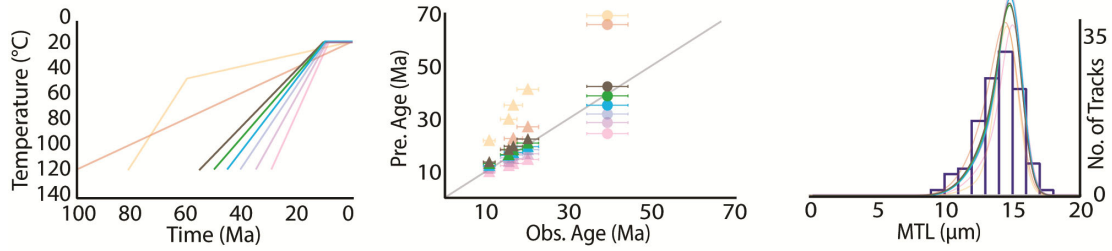


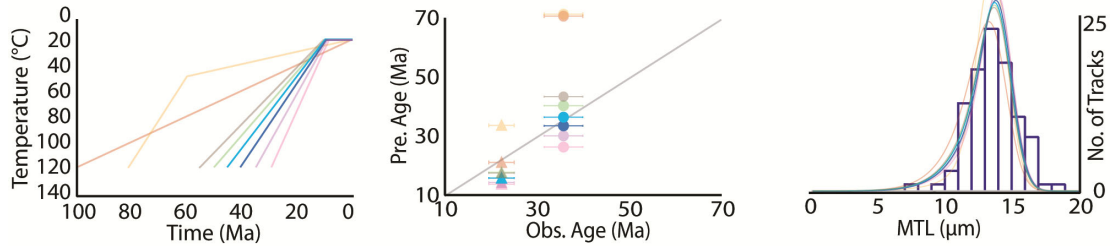
Figure DR7. Joint inverse thermal history model of samples 11 and 12, collected at the top and base of the outcropping southern Lokichar Fault footwall, determined using $QTQt$ (Gallagher, 2012). The best-fit time-temperature paths (weighted mean of the posterior distribution; see Gallagher, 2012 for discussion) are represented by dashed lines. Thin solid lines represent the 95% confidence interval limits. The data fit for the thermal history model is illustrated by panel inserts showing observed versus predicted thermochronology ages (circles = AFT; triangles = AHe) and observed confined track distributions overlain by the predicted distributions (blue curves) and the 95% confidence interval (grey curves) of the predicted distributions. See Thermal History Modelling for detailed modelling procedure and discussion.

Proximal Footwall Samples

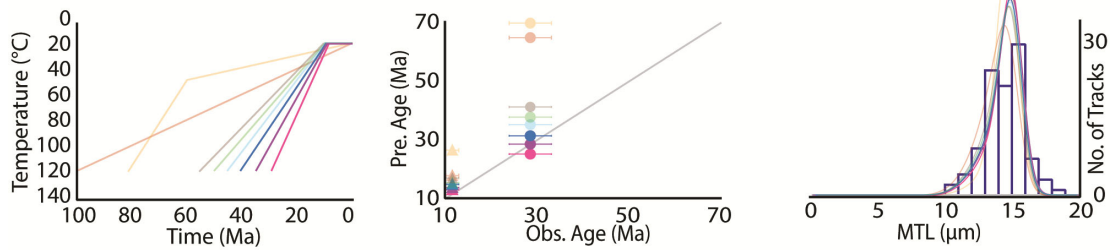
TUB16-11



TUB16-12

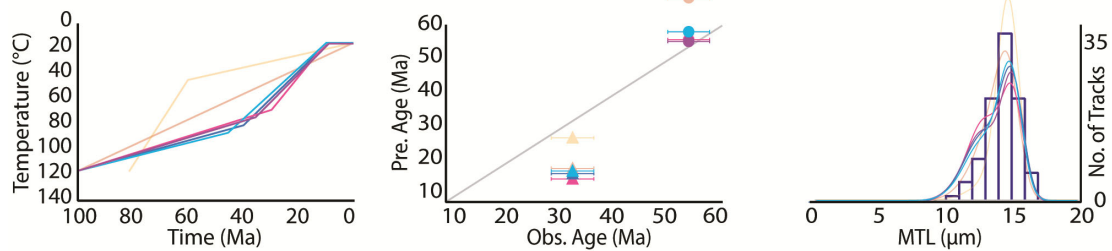


TUB16-14



Distal Footwall Samples

TUB16-07



TUB16-08

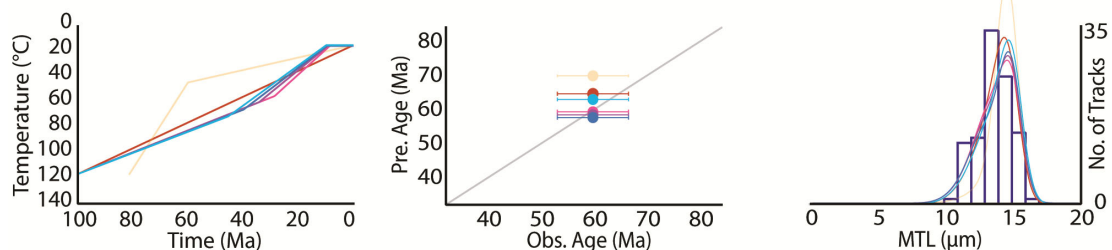
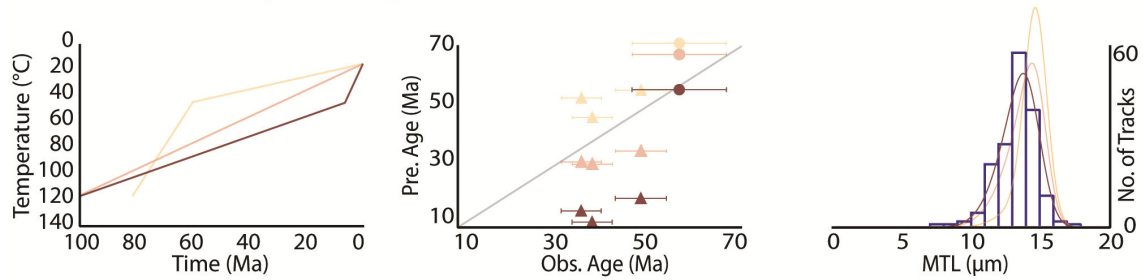


Figure DR8. Forward thermal history models of Lokichar Fault footwall samples with corresponding plots of observed versus predicted ages (circles = AFT; triangles = AHe) and observed confined track distributions overlain by the predicted distributions. Time-temperature histories unable to reproduce observed AFT age and confined track data are greyed out, along with their corresponding data. The only cooling history consistent with thermochronology data from both sample 11 and 12, collected at the top and base of the outcropping southern Lokichar Footwall, is that involving a 45 Ma onset of rapid cooling (Fig. DR4), consistent with their joint inverse thermal history model. Data from sample 14 agree with a later onset of rapid cooling between 40-30 Ma, consistent with inverse modelling results (cooling onset ~40 Ma). AFT and MTL data from samples 7 and 8 are consistent with gradual Late Cretaceous-Recent cooling followed by a transition to more rapid cooling ca. 45-30 Ma. No modelled cooling scenario is able to reproduce AHe data for sample 7. Undisturbed Late Cretaceous-Recent cooling is also able to reproduce the AFT data of sample 8 within error. See Thermal History Modelling for detailed modelling protocol and the main text for geological interpretation and discussion.

Hanging Wall Sample - TUB13-39

Monotonic & 2-Stage Cooling



Monotonic Cooling w/ Reheating Period

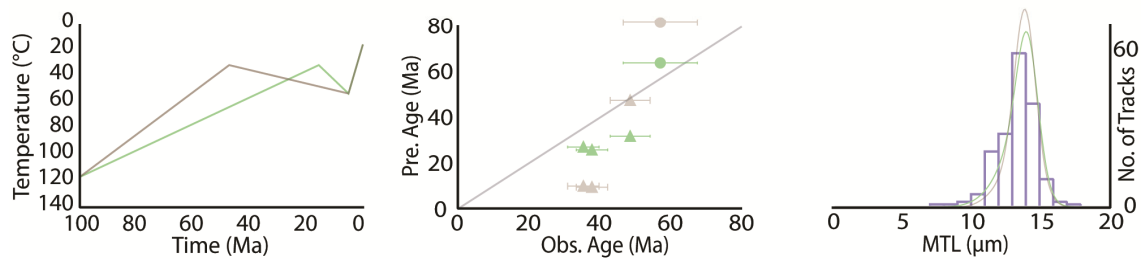


Figure DR9. Forward thermal history models of Lokichar Fault hanging wall sample (39) with corresponding plots of observed versus predicted ages (circles = AFT; triangles = AHe) and observed confined track distributions overlain by the predicted distributions. Time-temperature histories unable to reproduce observed AFT age and confined track data are greyed out, along with their corresponding data. Only prolonged Late Cretaceous-Miocene cooling followed by relatively rapid Pliocene-Recent cooling (maroon t-T path, top row) was able to reproduce both sample 39's AFT age and confined track distribution skewed towards shorter lengths. None of the prescribed thermal histories are able to reproduce any of the AHe data. See Thermal History Modelling for detailed modelling procedure and discussion.

REFERENCES

- Barbarand, J., Carter, A., Wood, I., & Hurford, T. (2003). Compositional and structural control of fission-track annealing in apatite. *Chemical Geology*, *198*(1–2), 107–137. [https://doi.org/10.1016/S0009-2541\(02\)00424-2](https://doi.org/10.1016/S0009-2541(02)00424-2)
- BEICIP. (1987). Geological Map of Kenya. Nairobi: Ministry of Energy and Regional Development.
- Boone, S. C., Seiler, C., Reid, A. J., Kohn, B., & Gleadow, A. (2016). An Upper Cretaceous paleo-aquifer system in the Eromanga Basin of the central Gawler Craton, South Australia: evidence from apatite fission track thermochronology. *Australian Journal of Earth Sciences*, *63*(3), 315–331. <https://doi.org/10.1080/08120099.2016.1199050>
- Brown, R. W., Beucher, R., Roper, S., Persano, C., Stuart, F., & Fitzgerald, P. (2013). Natural age dispersion arising from the analysis of broken crystals. Part I: Theoretical basis and implications for the apatite (U-Th)/He thermochronometer. *Geochimica et Cosmochimica Acta*, *122*(120), 478–497. <https://doi.org/10.1016/j.gca.2013.05.041>
- Farley, K. A., Wolf, R. A., & Silver, L. T. (1996). The effects of long alpha-stopping distances on (U-Th)/He ages. *Geochimica et Cosmochimica Acta*, *60*(21), 4223–4229. [https://doi.org/10.1016/S0016-7037\(96\)00193-7](https://doi.org/10.1016/S0016-7037(96)00193-7)
- Foster, D. A. (2019). Fission-Track Thermochronology in Structural Geology and Tectonic Studies. In M. G. Malusà and P. G. Fitzgerald (Eds.), *Fission-Track Thermochronology and its Application to Geology*. Springer, Berlin (pp. 211–220).
- Galbraith, R. F. (2005). *Statistics for fission track analysis*. Boca Raton: Taylor & Francis Group.
- Gallagher, K. (2012). Transdimensional inverse thermal history modeling for quantitative thermochronology. *Journal of Geophysical Research: Solid Earth*, *117*. <https://doi.org/10.1029/2011JB008825>
- Gallagher, K., Charvin, K., Nielsen, S., Sambridge, M., & Stephenson, J. (2009). Markov chain Monte Carlo (MCMC) sampling methods to determine optimal models, model resolution and model choice for Earth Science problems. *Marine and Petroleum Geology*, *26*, 525–535. <https://doi.org/10.1016/j.marpetgeo.2009.01.003>
- Gautheron, C., Tassan-Got, L., Barbarand, J., & Pagel, M. (2009). Effect of alpha-damage annealing on apatite (U-Th)/He thermochronology. *Chemical Geology*, *266*, 157–170. <https://doi.org/10.1016/j.chemgeo.2009.06.001>
- Gleadow, A. J. W., & Duddy, I. R. (1981). A Natural Long-Term Track Annealing Experiment for Apatite. *Nuclear Tracks*, *5*(1–2), 169–174.
- Gleadow, A., Harrison, M., Kohn, B., Lugo-zazueta, R., & Phillips, D. (2015). The Fish Canyon Tuff: A new look at an old low-temperature thermochronology standard. *Earth and Planetary Science Letters*, *424*, 95–108. <https://doi.org/10.1016/j.epsl.2015.05.003>
- Gleadow, A. J. W., Gleadow, S. J., Belton, D. X., Kohn, B. P., Krochmal, M. S., & Brown, R. W. (2009). Coincidence mapping – a key strategy for the automatic counting of fission tracks in natural minerals. *Geological Society of London Special Publications, Thermochronological Methods: From Palaeotemperature Constraints to Landscape Evolution Models.*, *324*, 25–36. <https://doi.org/10.1144/SP324.2>
- Hasebe, N., Barbarand, J., Jarvis, K., Carter, A., & Hurford, A. J. (2004). Apatite fission-track chronometry using laser ablation ICP-MS. *Chemical Geology*, *207*(3), 134–145.
- Ketcham, R. A., Carter, A., Donelick, R. A., Barbarand, J., & Hurford, A. J. (2007a). Improved modeling of fission-track annealing in apatite. *American Mineralogist*, *92*, 799–810. <https://doi.org/10.2138/am.2007.2281>
- Ketcham, R. A., Carter, A., Donelick, R. A., Barbarand, J., & Hurford, A. J. (2007b). Improved measurement of fission-track annealing in apatite using c-axis projection.

- American Mineralogist*, 92(5–6), 789–798. <https://doi.org/10.2138/am.2007.2280>
- McDowell, F. W., McIntosh, W. C., & Farley, K. A. (2005). A precise 40Ar - 39Ar reference age for the Durango apatite (U-Th)/He and fission track dating standard. *Chemical Geology*, 214(3), 249–263.
- Morley, C. K., Stone, D. M., Harper, R. M., & Wigger, S. T. (1999). Geology and Geophysics of the Western Turkana Basins, Kenya. In C. K. Morley (Ed.), *Geoscience of Rift Systems—Evolution of East Africa: AAPG Studies in Geology No. 44* (pp. 19–54).
- NASA. (2000). Shuttle Radar Topography Mission (SRTM) 1 Arc-Second Global. Sioux Falls, SD: Land Processes Distributed Active Archive Center. Retrieved from <http://lpdaac.usgs.gov>
- Paton, C., Hellstrom, J., Paul, B., Woodhead, J., & Hergt, J. (2011). Iolite: Freeware for the visualisation and processing of mass spectrometric data. *Journal of Analytical Atomic Spectrometry*, 26, 2508–2518. <https://doi.org/10.1039/c1ja10172b>
- Seiler, C., Kohn, B., & Gleadow, A. (2014). Apatite fission track analysis by LA-ICP-MS: An evaluation of the absolute dating approach. In *International Conference on Thermochronology*.
- Vermeesch, P. (2009). RadialPlotter: A Java application for fission track, luminescence and other radial plots. *Radiation Measurements*, 44(4), 409–410.
- Vermeesch, P. (2018). Chapter 6. Statistics for fission-track thermochronology. In (Ed.), *Fission-track thermochronology and its application to geology*. Springer, Berlin. .
- Wagner, G., & Van den Haute, P. (1992). *Fission-Track Dating*. Dordrecht: Kluwer Academic Publishers.
- Wildman, M., Brown, R., Beucher, R., Persano, C., Stuart, F., Gallagher, K., ... Carter, A. (2016). The chronology and tectonic style of landscape evolution along the elevated Atlantic continental margin of South Africa resolved by joint apatite fission track and (U-Th-Sm)/He thermochronology. *Tectonics*, 35(3), 511–545. <https://doi.org/10.1002/2015TC004042>